Polar cap size during 14–16 July 2000 (Bastille Day) solar coronal mass ejection event: MHD modeling and satellite imager observations

L. Rastätter, M. Hesse, M. Kuznetsova, and J. B. Sigwarth
NASA Goddard Space Flight Center, Greenbelt, Maryland, USA

J. Raeder
Space Science Center, University of New Hampshire, Durham, New Hampshire, USA

T. I. Gombosi
Department of Engineering, University of Michigan, Ann Arbor, Michigan, USA

Received 8 July 2004; revised 3 March 2005; accepted 22 March 2005; published 15 July 2005.

[1] This study investigates the development of the polar cap area as simulated by global magnetohydrodynamic models of the Earth's magnetosphere during the 14–16 July 2000 (Bastille Day) event. Around 1440 UT on 15 July, a magnetic cloud hit the magnetosphere and in the following hours high levels of activity in the magnetosphere and ionosphere were driven by the frequent changes in solar wind conditions. We compare the size of the polar cap (region of open magnetic field lines) as computed with two MHD models (UCLA-GGCM and BATSRUS) with observation data obtained from the IMAGE and Polar satellites. The two models in general reproduce the changes of the polar cap size that are seen by the satellite imagers. The range of modeled polar cap sizes, however, is limited to about 50–80% of the size range seen by the imagers and the shapes of the polar caps sometimes differ considerably among the models and compared to the observations. We found that a smoothing of solar wind parameters occurs, suggesting that solar wind inputs are stored in the magnetospheric system over a certain "memory" timescale. Cross-correlations are computed between smoothed solar wind input and the time history of the resulting polar cap size. Modeled magnetospheric "memory" timescales are estimated to be less than 12 min, whereas the satellite image data suggest a timescale of more than 20 min. The driver of magnetospheric activity in the models was found to be the B_z (north-south) component of the solar wind magnetic field and to a lesser degree, the Akasofu ϵ parameter which is closely related to B_z but is also influenced by the solar wind velocity V_x and magnetic field B_y. N, V_x, and $P_{\mathrm{dyn}} \propto NV_x^2$ show some degree of anticorrelation with observed polar cap sizes, but anticorrelations are barely significant for polar caps computed from either model. Memory timescales and reaction time delays could be derived from some of the parameters within the limits of statistical significance of the correlation coefficients.

Citation: Rastätter, L., M. Hesse, M. Kuznetsova, J. B. Sigwarth, J. Raeder, and T. I. Gombosi (2005), Polar cap size during 14–16 July 2000 (Bastille Day) solar coronal mass ejection event: MHD modeling and satellite imager observations, *J. Geophys. Res.*, *110*, A07212, doi:10.1029/2004JA010672.

1. Introduction

[2] The 15 July 2000 event produced a series of disturbances that eventually lead to a large storm event on 15 July. In this work, we concentrate on the events of 15 July after 1400 UT which are characterized by the first impact of a CME structure at 1438 UT. This is followed by structures passing throughout the following 4 hours through a southward turning of the interplanetary magnetic field (IMF) B_z after 1900 UT and a slow decay of the IMF until midnight.

[3] Of fundamental importance for the plasma and energy transport between the solar wind and the Earth's magnetosphere down to the ionosphere is the magnetic configuration, especially the location and extent of open magnetic field lines connected to the polar regions of the Earth and the solar wind which allow direct particle transfer from the solar wind. Aviation and space flight in high-latitude regions are affected by high radiation levels during storm events and predictions of possible dangers are needed.

0148-0227/05/2004JA010672$09.00

Theoretical theories of the magnetic field's role [*Dungey*, 1961; *Axford and Hines*, 1961] describe magnetic reconnection and viscous interaction as the main modes of plasma transfer into the magnetosphere. Reconnection is responsible for the topological changes that allow the amount of open magnetic flux in the Earth polar regions to change with the changing rates of dayside and nightside reconnection [*McPherron*, 1991]. Earlier simulation studies have depicted magnetic field lines and their connectivity for different IMF conditions [*Walker et al.*, 1993; *Raeder*, 1999] including the event that is studied in this paper [*Raeder et al.*, 2001c]. This is a first quantitative comparison between the time-dependent change of the polar cap size simulated with two global MHD models and data obtained from satellite imager data. We use data from the IMAGE Wideband Imaging Camera (WIC) [*Mende et al.*, 2001; *Mende et al.*, 2003] and the Polar Visible Imaging System (VIS) Earth Camera [*Frank et al.*, 1999; *Frank and Sigwarth*, 2003] to estimate the polar cap size as defined by the poleward edge of auroral emission in near- and far-ultraviolet light due to precipitating particles in the boundary layer of closed field lines of the inner magnetosphere. The magnetospheric magnetohydrodynamic (MHD) simulation models that have been run for the same time period are the UCLA-GGCM model [*Raeder*, 1999; *Raeder et al.*, 2001b] and the BATSRUS model [*Powell et al.*, 1999; *Gombosi et al.*, 2002].

[4] This is a follow-up study of the three-dimensional (3-D) configuration studied [*Rastätter et al.*, 2002] which focused on the 3-D magnetic field structure in the magnetosphere and the effects on the magnetic mapping between the the ionospheric hemispheres. This study focuses on the performance of numerical simulation of the Earth's magnetosphere with emphasis on the polar caps in the polar ionosphere. We shall address the following questions: (1) How do global MHD models reproduce the polar cap (size, shape, and location) seen by satellite imagers and how do the model results depend on ionospheric conductances? (2) What are reaction times to changes in the solar wind for observed and modeled polar cap sizes? (3) What parameter in the solar wind acts as the primary driver of the polar cap size and shape in the observations and the models?

[5] The paper is organized as follows. After a brief explanation of the models in section 2, we present an overview of the solar wind and IMF conditions in section 3, the satellite imager data in section 4, and the model results in section 5. Section 6 presents the cross-correlation results. Finally, section 7 summarizes and discusses the findings and implications.

2. MHD Models

[6] The dimensionless MHD equations are given by

$$\frac{\partial \rho}{\partial t} = -\nabla \cdot (\rho \mathbf{V}) \tag{1}$$

$$\frac{\partial \rho}{\partial \mathbf{V}} t = -\nabla \cdot (\rho \mathbf{V}\mathbf{V} + \mathrm{p}\mathbf{I}) + \mathbf{J} \times \mathbf{B} \tag{2}$$

$$\frac{\partial e}{\partial t} = -\nabla \cdot [(e+p)\mathbf{V}] + \mathbf{J} \cdot \mathbf{E} \tag{3}$$

$$e = \frac{1}{2}\rho V^2 + \frac{p}{\gamma - 1} \tag{4}$$

$$\frac{\partial \mathbf{B}}{\partial t} = -\nabla \times \mathbf{E} \tag{5}$$

$$\mathbf{E} = -\mathbf{V} \times \mathbf{B} + \eta \mathbf{J} \tag{6}$$

$$\mathbf{J} = \nabla \times \mathbf{B}. \tag{7}$$

$$\nabla \cdot \mathbf{B} = 0. \tag{8}$$

The symbols have their usual meanings: **B** is the magnetic field, **E** is the electric field, ρ is the mass density, **V** is the plasma velocity, p is the plasma pressure, **J** is the current density, e is the plasma energy density, and $\gamma = 5/3$ is the ratio of specific heats assumed in all simulations. Magnetic field and plasma density are normalized to typical fields B_0 (say, $\sim$10 nT) and densities ρ_0 (5 protons per cm^3) found in the solar wind (e.g., at the start time of a simulation). Pressures are normalized to the magnetic pressure $P_0 = B_0^2/(2\mu_0) \sim 0.04$ nPa, velocities are normalized to the resulting Alfvén velocity $V_A = B(\mu_0\rho_0)^{-0.5} \sim 98$ km/s. Normalization of current densities follows from that of B using the length scale $L = 1R_E$ (one Earth radius): $J_0 = B_0/(\mu_0 L) \sim 1.25$ nA/m^2.

[7] The coordinates X, Y, and Z correspond to X_{GSE}, Y_{GSE}, and Z_{GSE} for the UCLA-GGCM model and X_{GSM}, Y_{GSM}, and Z_{GSM} for BATSRUS. The finest grid resolution near the Earth is 0.25 R_E for both models.

[8] The UCLA-GGCM model uses the MHD equations in the above form with nonconservative source terms for the magnetic forces in equations (2) and (3) [*Raeder*, 2003] and employs a high-order finite difference scheme. BATSRUS, however, uses fully conservative equations and employs a split $\mathbf{B} = \mathbf{B_0} + \mathbf{B_1}$ with $\mathbf{B_0}$ being the analytically defined Earth dipole field and $\mathbf{B_1}$ the first-order (time-varying) part of the magnetic field [*Powell et al.*, 1999; *Gombosi et al.*, 2002].

[9] BATSRUS uses a finite-volume approximate Riemann solver scheme and ideal MHD ($\eta = 0$) and relies on flux limiters to provide numerical stability by eliminating numerical noise [*Gombosi et al.*, 2002]. In addition to TVD and constrained transport schemes that provide numerical stability, the UCLA-GGCM model employs a current-dependent localized resistivity model in the magnetosphere outside 6 R_E:

$$\eta = \alpha H(j\prime - \delta)(j\prime)^2 \tag{9}$$

$$j\prime = \frac{|J|d}{|B| + \epsilon}, \tag{10}$$

where H is the Heaviside function and j' is the normalized current density calculated with the local magnetic field B,

the grid spacing d, and a very small positive number ϵ to avoid divisions by zero. Parameters α and δ are 0.65 and 0.05, respectively. These parameters are standard selections that provide a dynamic tail [*Raeder et al.*, 2001a].

[10] Both models use flux limiters to prevent unphysical overshoots and to stabilize the numerical time advance and the MHD equations are solved in a semirelativistic approximation, a form of the Boris correction [*Boris*, 1970]. A reduced speed of light of c_{boris} = 3000 km/s speeds up the explicit time integration used by the models by reducing the fastest phase velocity in the semirelativistic system. For an in-depth discussion on the equations and solution methods, see *Powell et al.* [1999] and *Gombosi et al.* [2001] for BATSRUS and *Raeder et al.* [2001a, 2001b] and *Raeder* [2003] for the UCLA-GGCM model.

[11] The upstream inflow boundary (at $X = 33R_E$) is updated with IMF data from the Geotail magnetic field instrument (MGI) [*Kokubun et al.*, 1994] and plasma density and temperature data from the plasma instrument (CPI) [*Frank et al.*, 1994] obtained through CDAWeb (64-s data, see Figure 3). Geotail was located at about 24 R_E upstream of the Earth, near the inflow boundary at 33 R_E, so the solar wind data do not have to be propagated toward the boundary. The other boundaries (at $Y = \pm 96$ and $Z = \pm 96$ for BATSRUS and $Y = \pm 64$ and $Z = \pm 64$ for UCLA-GGCM) have zero-gradient boundary conditions. Outflow boundary conditions are specified at the far-tail end ($X = -351R_E$) of the simulation box. The inner boundary of the magnetospheric MHD simulations is located at 3 R_E from the Earth to avoid the extremely high magnetic field and high Alfvén speeds close to the Earth.

[12] The MHD portions of the models are coupled to an ionospheric conductance model and electric potential solver to obtain self-consistent plasma flow (electric field) boundary conditions at this inner boundary. The field-aligned currents (FAC) are mapped from the magnetosphere at 4 R_E onto the ionosphere using an analytic magnetic field model. For the BATSRUS model, the field model is a tilted dipole in GSM coordinates with the tilt being updated throughout the simulation. For UCLA-GGCM, the dipole field orientation in GSE coordinates remains fixed at the position of the dipole at 1900 UT (in the middle of the simulated time period). The FAC are converted into radial currents J_R that feed a two-dimensional surface electrodynamics model using Hall- and Pedersen conductances that either depend on solar irradiation and the incoming magnetospheric currents (runs marked "BATSRUS auroral" [*Gombosi et al.*, 2002] and "UCLA-GGCM CTIM" [*Raeder et al.*, 2001b]) or are set to constant Hall and Pedersen conductances of 10 S (runs marked "$\Sigma = 10$" with both models). The electric potential solution is converted to a plasma flow velocity using $\mathbf{E} = -\nabla\Phi$ together with $\mathbf{E} = -\mathbf{V} \times \mathbf{B}$. V is mapped back to cells within the 3 R_E boundary for the MHD part of the simulation. The procedure is described in detail, for example, by *Goodman* [1995]. The $F10.7$ parameter, whose value was 217 for 15 July 2000, parameterizes the solar EUV and UV radiation and is used as input to the ionosphere models. It critically affects the ionospheric conductances on the sunlit dayside. [e.g., *Hedin*, 1987; *Bailey and Balan*, 1996; *Roble and Ridley*, 1994]. Conductances range up to 27.9 S for Hall and 19 S for Pedersen conductivities in the dayside. In the UCLA-GGCM model the ionospheric conductances are set constant or are self-consistently determined by the CTIM model coupled to the MHD magnetosphere. In BATSRUS, an auroral conductance pattern ("Σ_{aurora}") depending on FAC derived by a statistical model [*Ridley et al.*, 2001] is then added to the background conductances using the sum-of-squares rule ($\Sigma = (\Sigma^2_{\text{back}} + \Sigma^2_{\text{dayside}} + \Sigma^2_{\text{aurora}})^{0.5}$) for each (Pedersen and Hall) conductance.

[13] MHD simulations were performed for the time period (1300 UT to 2400 UT on 15 July 2000). As an initial condition, BATSRUS fills the simulation box with the solar wind plasma density, flow velocity, and interplanetary magnetic field (IMF) conditions at the specified start time (1300 UT) and adds the tilted dipole field. In a setup phase a stationary state is computed from the initial state forming the near-Earth magnetosphere, magnetosheath, and magnetotail structures. After the setup phase the time-dependent simulation is started. With the upstream boundary at 33 R_E and typical solar wind velocity of -600–-1000 km/s the real solar wind conditions arrive at Earth in about 4–5 min after passing the boundary. Realistic magnetospheric and magnetotail conditions are expected to be assumed within 10–15 min after start of the time-dependent simulation.

[14] The UCLA-GGCM model simulation also starts off with a tilted dipole. The magnetosphere is filled with a uniform plasma density moving with the initial solar wind speed outside a certain radius from the Earth (3 times the inner radius, about 9 R_E). The magnetotail then forms during a 2-hour startup period with constant solar wind conditions (i.e, from 1100 UT to 1300 UT). In addition to the two models' startup procedures, an additional hour of simulation time from 1300 UT to 1400 UT allows the models to adjust fully to the quiet-time solar wind conditions. The analyses described in this paper only include model results after 1400 UT.

3. Solar Wind and IMF Conditions

[15] Figure 3 shows the solar wind input during the time period of 1300 UT to 2400 UT with the major changes in the solar wind indicated by the vertical lines. The first shock at the leading edge of the sheath of shocked interplanetary material surrounding the magnetic cloud that arrives later on 15 July 2000 can be seen at the Geotail satellite around 1436 UT, about 4 hours before the main magnetic cloud itself arrives at around 1930 UT. The cloud is identified in different ways, e.g., as "Cloud 4" [*Smith et al.*, 2001] or "magnetic cloud 2" (MC2) [*Lepping et al.*, 2001] in the literature on this event. Strong inner magnetospheric and ionospheric reactions are seen in response to the solar wind disturbances as the sheath and the cloud pass the Earth, [e.g., *Liu et al.*, 2001; *Jordanova et al.*, 2001]. The polar cap size changes are seen by the imagers on board of the IMAGE and Polar satellites shortly afterward.

[16] The impact changes IMF conditions from a quiet-time $B_z = -5$ nT, $B_y = 3$ nT and N = 3–7 cm^{-3} to B_y, $B_z \sim 20$ nT, $N \sim 20$–25 cm^{-3}. The density peaks 20 min later at $\sim$38 cm^{-3} and declines to previous levels from there. Between 30 and 42 min after impact (1506–1518 UT) the magnetic field component B_y reverse sign from $\sim$25 nT to ~ -20 nT. B_z shows a transient increase above 20 nT up to

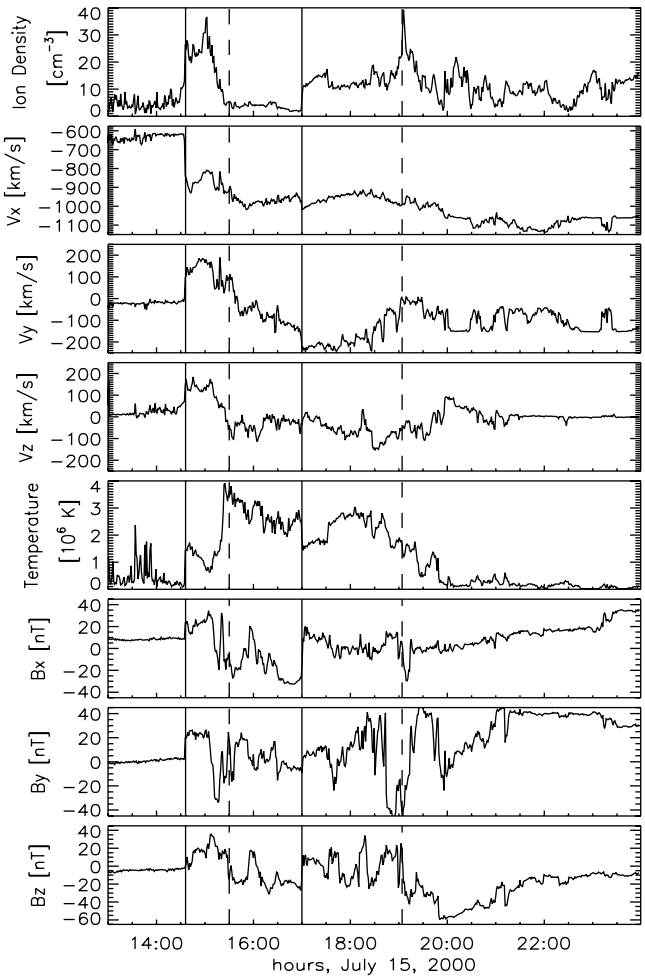

Figure 1. Solar wind input. For the period from 1300 UT to 2400 UT the solar wind parameters used for the simulation are shown. The vertical bars show the time periods that are mentioned in this paper (solid lines represent 1428 UT and 1700 UT; dashed lines represent 1530 UT and 1904 UT). Shown are the plasma density, temperature, velocity components, and magnetic field components measured by Geotail located at about X = 24 R_E and close to the Sun-Earth line in the solar wind.

$\sim$35 nT during this 12-min period but otherwise remains at the level of $\sim$15 nT.

[17] The tailing edge of the first structure of the CME sheath passes the satellite at around 1530 (first dashed line) and a period of negative B_z lasts until 1700 UT (second solid line). Varying IMF B_z and strong B_y IMF conditions prevail until about 1904 UT (second dashed line), followed by a period of strong negative B_z in the CME-proper [*Lepping et al.*, 2001; *Smith et al.*, 2001] (nearly -60 nT around 2000 UT, notice that the scale differs from those for the B_x and B_y plots). The negative B_z slowly decays to ~ -1 nT at midnight.

[18] Although the IMF B_x is not always small in comparison with B_y and B_z (see Figure 3), B_x is set to zero throughout the setup and all the time-dependent simulations as $\nabla \cdot \mathbf{B} = \mathbf{0}$ has to be fulfilled at the upstream boundary and gradients of B_y and B_z within the upstream Y, Z-plane are unknown. A minimum variance approach that defines a fixed orientation of magnetic layers in the solar wind throughout the simulation time interval [*Sonnerup and Cahill*, 1967; *Sonnerup and Cahill*, 1968] was not deemed appropriate for this long time interval during which the orientation of magnetic layers in the solar wind changes significantly. Most of the time, B_x is not dominating the field components B_y and B_z and may be neglected [*Raeder et al.*, 2001a].

4. Satellite Imager Data

[19] The black lines in Figure 2 show the polar cap size as computed from the poleward edge of the auroral emissions measured by the two satellites' imagers. The determination of the polar cap edge is the same as in the work of *Frank and Craven* [1988, p. 260]. The beginning of the time period is covered by the IMAGE instrument (solid line) the later times are covered by the Polar satellite's imager (dashed line). The overlap period of $\sim$38 min from 1705 UT to 1743 UT shows the good agreement between the analyses of the two imagers' data. We believe that this indicates that both data sources show essentially the same features that can be compared with modeled results. For purposes of this paper, a single time line of measured polar cap sizes is derived by switching over from IMAGE data to Polar data at the middle of the overlap interval (1720 UT).

[20] The IMAGE FUV satellite data represent images taken at a broad spectrum of wavelengths in the far ultraviolet that is attributed to an approximate emission height of 120 km. The poleward boundary of the combined emissions from precipitating electrons and ions is taken as an observational estimate of the polar cap region. Emissions recorded by Polar VIS are assumed to emanate from an

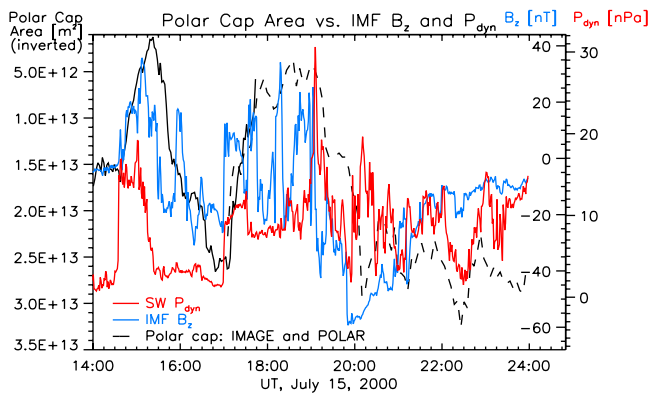

Figure 2. Polar cap sizes from satellite observations and model runs in comparison with solar wind B_z and P_{dyn}. Observations of polar caps (solid black line represents IMAGE, while dashed line represents Polar), solar wind B_z (blue) and solar wind dynamic pressure P_{dyn} (red) from 1400 UT to 2400 UT on 15 July 2000. One can see the response of the polar cap size to the IMF B_z with a small time delay. The dynamic pressure appears as a trigger to changes of the polar cap size as well, especially after 2100 UT where the cap sizes follow changes of P_{dyn} very closely.

altitude of 200 km and represent the VIS instrument's near-ultraviolet spectral range.

[21] The satellite observations provide an outline of the polar cap area at 100 positions around the auroral region. These positions have been analyzed to provide the surface area of the caps (in m^2) and the geomagnetic positions of the boundary points can be plotted in comparison with the modeled results. The analysis method for both imager data is essentially the same. The polar cap is defined as the region near the pole from which emissions are less than a small threshold percentage of the auroral emission intensity after correction for scattered daylight. A global reduction of the polar cap size is seen by both IMAGE and Polar in the overlap time period, although the two instruments use different wavelengths and the analysis assumes different emission altitudes.

[22] In addition to the observed polar cap size, Figure 2 shows the IMF B_z (blue line) and the solar wind dynamic pressure $P_{\mathrm{dyn}} = \frac{\rho}{2} V_x^2$ (red line). The periods of northward IMF B_z are associated with decreasing polar cap sizes (between 1438 and 1500 UT and 1705 to 1910 UT), whereas increasing polar cap sizes are observed in periods when B_z is negative as expected from magnetic reconnection occurring at the cusps ($B_z > 0$) or at lower latitudes near the subsolar point ($B_z < 0$), respectively [*McPherron*, 1991]. The dynamic range of those changes is quite large due to the magnitude of the IMF in either direction and current polar cap size clearly depends on the history of B_z (as quantified in the cross-correlation section in this paper). The later evolution of the polar cap size (after 2000 UT) is characterized by geomagnetic activity with a strong negative B_z with decreasing intensity until midnight.

[23] The first northward IMF B_z period reduces the polar cap from the quiet-time size of $\sim 1.5 \cdot 10^{13}$ m^2 before 1438 UT to less than 10% of the quiet-time size at 1520 UT ($\sim 10^{12}$ m^2). Later in the evolution the polar cap as seen by the imager increases in size and eventually reaches a size larger than the original size by 1545 UT. Periods with intense southward B_z yield maximum polar cap sizes of $2.55 \cdot 10^{13}$ m^2 around 1700 UT and $2.8 \cdot 10^{13}$ m^2 is exceeded repeatedly after 2000 UT.

[24] The solar wind dynamic pressure may influence the polar cap sizes in addition to the IMF B_z. Early during the day, P_{dyn} triggers polar cap changes in combination with the IMF B_z. During the time of southward IMF B_z between about 2045 UT and 2330 UT the polar cap size seen by Polar tracks changes of the dynamic pressure very closely.

5. Simulation Results

[25] The size and shape of the polar cap is defined by the magnetic flux that is associated with "open" magnetic field lines, those that connect the Earth's polar regions to the interplanetary magnetic field. Magnetospheric and magnetotail field lines, however, are "closed" if they connect the northern hemisphere with the southern hemisphere through magnetic field lines carrying plasma of the inner magnetosphere or the tail plasma sheet. The transition of a field line from "closed" to "open" occurs through magnetic reconnection near the subsolar point of the magnetopause with southward IMF or at the cusps above the polar regions with northward IMF. For other IMF clock angles the location of strongest reconnection lies on the dawnside or duskside depending on the IMF B_y. The rate of reconnection along the dayside in comparison with the nightside reconnection (in the magnetotail) will determine the amount of open flux changes seen in the polar caps. The purpose of this study is to investigate the open flux changes during the Bastille Day event and to verify whether MHD models such as UCLA-GGCM and BATSRUS are able to represent these changes adequately.

[26] To generate the polar cap size from the MHD simulations, a grid of 61 by 61 footpoints is imposed onto the northern hemisphere with X_{SM} and Y_{SM} ranging from -0.577 R_E to 0.577 R_E covering an area of more than 35 degrees from the magnetic pole with resolution of about 1.1 degrees. The position in Z_{SM} is then calculated to match the ionospheric height of 90 km. This resulting position in SM coordinates is then mapped along dipolar field lines to the near-Earth boundary of the MHD simulation ($3R_E$) and transformed into GSM (BATSRUS) or GSE (UCLA-GGCM) coordinates to yield the field line start points in the magnetosphere. Field lines that then do not return back to the near-Earth boundary are considered open and contribute to the polar cap. The size of the cap is obtained by summing up the surface areas in the grid which contain open field lines. The near-Earth boundary of the MHD simulations at $R_0 = 3$ R_E ensures that the area covered by the field line footpoints, $A = 2\pi R_E^2 \int_0^{\theta_0} \sin(\theta)\, d\theta = 2\pi R_E^2 (1 - \cos(\theta_0)) \sim 4.7 \cdot 10^{13}$ m^2 with $\theta_0 = \arcsin(R_0^{-0.5}) \sim 35°$, is large enough to cover the polar cap sizes seen during this event.

[27] The colored lines in Figure 3 show the polar cap sizes calculated from the satellite images (black line) and the polar cap sizes calculated from the simulation runs with the two models (blue and green represent BATSRUS with auroral and constant ionospheric conductances $\Sigma_P = \Sigma_H = 10$, respectively; red and orange represent UCLA-GGCM with CTIM and constant conductances, respectively). The modeled polar cap never reaches the small size seen by the imager data at 1516 UT and also generally remains lower than the observed extremes, except for a brief time period with the BATSRUS model run between 2000 and 2020 UT. The explanation for this damped behavior is that the balance between the magnetopause reconnection rate and the tail reconnection rate appears not to vary as much as in nature. This feature of MHD simulations has been seen before and the reasons are not clear [*Raeder et al.*, 2001b].

[28] For the BATSRUS model, the differences in the cap size for different ionospheric conductances are very small, whereas the results from the UCLA-GGCM model runs vary considerably, especially in the later phase (after 1900 UT) of the simulations.

[29] The pre-CME period (before 1430 UT) is characterized by a nearly constant IMF. All model runs reproduce nearly constant polar cap sizes which are slightly (up to 15%) smaller than observed by the IMAGE satellite (at 1420 UT). After the impact of the first CME, the modeled polar caps decrease in size, almost in the same timescale as the observations, albeit with only 1/2 to 2/3 of the amplitude (of about $14 \cdot 10^{13} m^2$) seen by the imager. After the temporary recovery at 1600 UT, the observed and modeled cap sizes coincide, only to be followed by a transient sharp

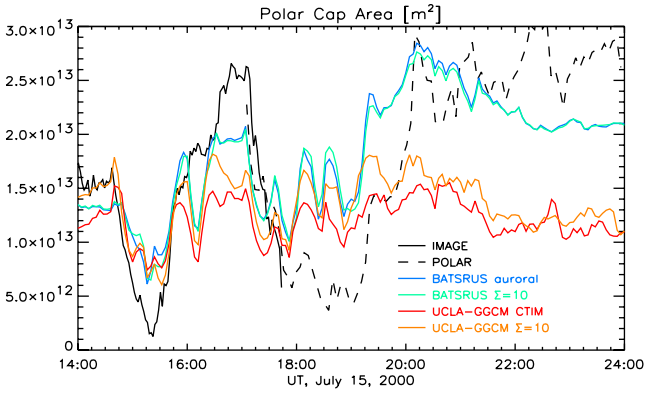

Figure 3. Observed and modeled polar cap sizes. The polar cap sizes computed from the MHD simulations with the two models (colored lines, two per model for different ionosphere conductances) are plotted in comparison to the observational data (black lines). The colors represent the following: blue is BATSRUS with auroral conductances, green is BATSRUS with $\Sigma_P = \Sigma_H = 10$ *S*, red is UCLA-GGCM with CTIM (conductances similar to BATSRUS' "auroral" model), and orange is UCLA-GGCM with $\Sigma_P = \Sigma_H = 10$ *S*.

drop in the modeled cap sizes (1600 UT to 1620 UT). The large increase between 1620 UT and 1700 UT is followed by the modeled polar caps, albeit with a much smaller range of change. Starting at 1700 UT, polar cap sizes shrink rapidly in the observations. All modeled polar caps also shrink at the same time but the shrinkage stops earlier than the change of the observed cap size. Although the model runs start from different polar cap sizes at 1700 UT ($\sim 2.0 \cdot 10^{13}$ m^2 for BATSRUS runs, $\sim 1.4 \cdot 10^{13}$ m^2 for the UCLA-GGCM runs), the reduction of the polar cap size is fairly similar for all model runs (about $\sim 8.0 \cdot 10^{12}$ m^2 until 1720 UT). Between 1720 UT and 1900 UT we see that smaller variations in the polar cap size are tracked in a very similar manner by all the model runs with a high degree of correlation to the observed polar cap sizes.

[30] After about 1930 UT the modeled polar cap sizes and the observations show very different behavior. All the model runs stop tracking the small periodic changes of the observed polar cap sizes and the difference in polar cap sizes seen by the UCLA-GGCM runs compared to the BATSRUS runs increases to 10^{13} m^2 from the previous level of an average of about $5 \cdot 10^{12}$ m^2. This time of intense substorm activity that is seen in the periodic changes of the observed polar caps after 2000 UT is notoriously difficult to model and the two models are behaving differently due to their different design. A test run of the UCLA-GGCM model with a constant magnetospheric resistivity (Lundquist number of 10^5, not shown) more closely resembles the behavior of the BATSRUS runs, suggesting that the BATSRUS runs correspond to an effective resistivity of approximately that value.

[31] We also find that the modeled magnetosphere acts like a low-pass filter that smoothes out fluctuations on short timescales (up to a few minutes). Compared to the satellite data one finds that the modeled polar cap sizes are much better correlated with B_z than the observed polar cap sizes as outlined in the correlation study below.

[32] The polar cap size during near-zero IMF B_z conditions agrees well with satellite imager observations as seen from the beginning of the modeled time interval (before 1430 UT). As B_z turns north the decrease of the polar cap size as calculated by the MHD models is weaker than the observations show. The rate of change of the polar cap size is comparable but lasts for a shorter time in the simulations. A prolonged period of negative IMF B_z fed into the MHD model for the later time periods does not yield the large polar caps as seen by the imagers. Both models exhibit a smaller range of possible polar cap sizes for this time period than is seen in the observation data.

6. Correlations

[33] In this section we shall quantify the impressions outlined in the previous section. We examine the cross-correlation between measured polar cap sizes, and modeled polar cap sizes and various solar wind parameters, such as the IMF B_z, solar wind V_x, the Akasofu ϵ, and the plasma dynamic pressure P_{dyn}.

[34] Cross-correlations *XC* measure the degree of similarity between two time series $F(t)$ and $G(t')$ in the time interval between T_0 and T_1. Coefficients calculated for different time shifts Δ between t and $t' = t - \Delta$ gives probable time delays between impacts of solar wind features and the corresponding magnetospheric responses:

$$XC(F(t), G(d, t-\Delta)) = \frac{\int_{T_0}^{T_1} [F(\tau) - \bar{F})][G(d, \tau - \Delta) - \bar{G}]\mathrm{d}\tau}{(T_1 - T_0)\,\sigma(F(t))\,\sigma(G(d, t-\Delta))} \tag{11}$$

$$\sigma(F(t)) = \left(\frac{1}{T_1 - T_0}\int_{T_0}^{T_1} [F(\tau) - \bar{F}]^2 \mathrm{d}\tau\right)^{\frac{1}{2}} \tag{12}$$

$$\sigma(G(B_z, d, t-\Delta)) = \left(\frac{1}{T_1 - T_0}\int_{T_0-\Delta}^{T_1-\Delta} [G(d, \tau) - \bar{G}]^2 \mathrm{d}\tau\right)^{\frac{1}{2}} \tag{13}$$

$$G(B_z, d, t = \int_{-\infty}^{0} \epsilon^{\tau/d} B_z(t-\tau) d\tau \tag{14}$$

where $\bar{F}$ is the mean of $F(t)$ in the time interval $T_0 < t < T_1$ and $\bar{G}$ is the mean of $G(B_z, d, t)$ in the shifted interval $T_0 - \Delta < t < T_1 - \Delta$. The parameter d in functional G is the timescale of the exponential smoothing of a solar wind parameter to account for the "memory" effect exhibited by the magnetosphere-ionosphere system (equation (14)). In equation (14), $G(B_z, d, t)$ is the smoothed solar wind parameter B_z with memory time d that is then compared to the polar cap data. In the limit of vanishing decay time d, $G(B_z, 0, t)$ is identical to the original time series of B_z. Any other solar wind parameter (V_x, ϵ, or P_{dyn}) can be used instead of B_z in the functional G. $F(t)$ stands for any of the modeled or observed polar cap data.

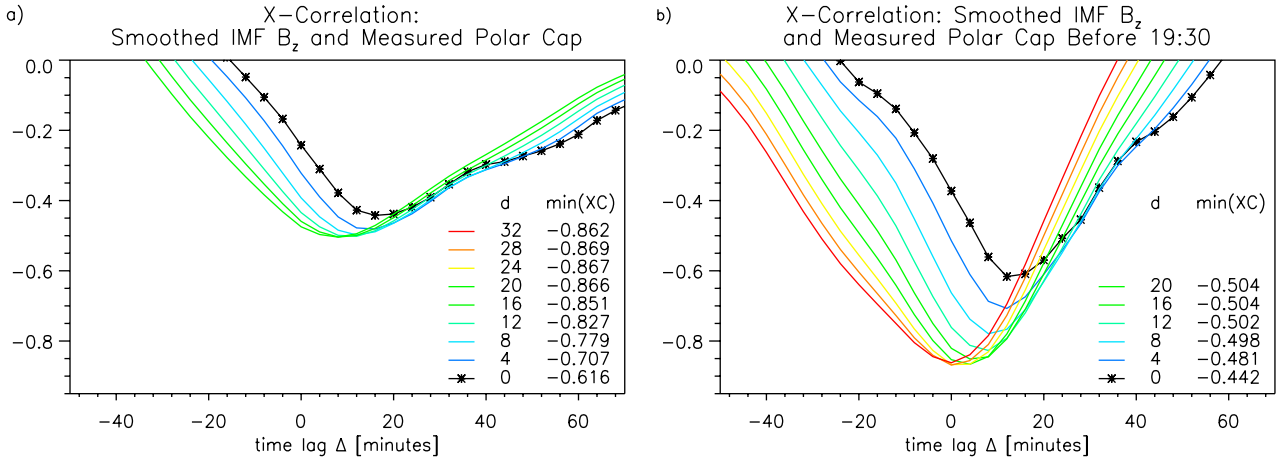

Figure 4. Cross-correlation of smoothed B_z and observed polar cap sizes. For the period from (a) 1400 UT to 2400 UT and (b) 1400 UT to 2400 UT the solar wind B_z and the combined IMAGE and Polar observations are used to calculate the coefficients. IMF B_z smoothing timescales $0 < d < 32$ min (nine colors) and time lags between −50 and +70 minutes were used for the plots. The distribution of the correlation coefficients shows a flat minimum that shifts to negative Δ with larger smoothing time d. Statistically significant correlations are obtained for $d \leq 20$ (Figure 4a) and for all values of d (Figure 4b). The correlations for the shorter period (Figure 4b) show more pronounced peaks.

[35] We evaluate the integrals as sums over the discrete number of samples equally spaced in time (interval δ = 4 min). The smoothing operation 14 is implemented by starting with $G(B_z, d, t = T_0) = B_z(T_0)$ at the beginning and by calculating $G(B_z, d, t) = e^{-\delta/d}\, G(B_z, d, t - \delta) + B_z(t)$ throughout the array of sample times until the end of the time period T_1 is reached. Observations (solar wind and polar cap sizes) were interpolated onto the sampling times (i.e., times of the models' outputs every 4 min).

[36] In the cross-correlation plots described below, the resulting coefficients are plotted with the time-lag Δ on the horizontal axis. The decay times d are represented by the color of the curves. Figure 4a shows the cross-correlation between the smoothed IMF B_z with various memory times d and the observed polar cap size in the northern hemisphere for the entire time period between 1400 UT and 2400 UT. The minimum of the cross-correlations decrease with larger d showing that there is a certain "memory" in the magnetosphere, i.e., the current state of the magnetosphere depends on many minutes' worth of previously encountered IMF conditions.

[37] However, the minimum at a level of $d = -0.504$ for $d = 16$ and $d = 20$ shown is not pronounced which indicates that the memory effect may be varying for different parts of the event. Curves for larger d ($\min(XC) \sim -0.502$) are not shown because statistical significance is lost. To check that hypothesis, we excluded the time after 1930 UT when time series plots in Figure 2 indicate a change of behavior of the model results (which follow B_z much more closely) compared with the measured polar cap sizes. Figure 4b shows the cross-correlation between the IMF B_z and the observed polar cap size in the northern hemisphere for the time period before about 1930 UT. In both parts we see that with increased memory time d the time lag at the minimum of XC decreases as the average age of the IMF B_z contributing to the integrated value G increases.

[38] We now compare the IMF B_z with the same range of memory times d to the modeled polar cap sizes in Figure 5 for one run with each model. Figure 5a shows the correlation between the IMF B_z smoothed with varying timescales d and the simulated polar cap size results from the BATSRUS model run with auroral conductances. The run with conductances of 10 S yields nearly identical cap sizes and is not shown. Figure 5b shows the same for the UCLA-GGCM model run with CTIM conductances in the ionosphere. In the time period before 1930 UT, the run with constant 10 S conductances does not differ too much from this run. The ionospheric conductance does not seem to play a significant role in the time evolution of polar cap sizes.

[39] Correlations XC with a smoothed input have to be tested for significance against the null hypothesis $XC \sim 0$. For a random test function, the autocorrelation is unity for zero shifts Δ and close to zero ($|XC| < 1.96/\sqrt{N}$ for 95% of the coefficients) for all other time shifts with for a discrete set of N samples. Adding the exponential smoothing increases autocorrelation coefficients for nonzero lags and change the statistical properties of the distribution of cross-correlation coefficients. The statistic

$$T_{XC} = XC\left(\frac{\mathrm{DoF}}{(1 - XC^2)}\right)^{0.5} \tag{15}$$

has a T-distribution [*Hauptmann*, 1994] with a "Degree of Freedom" (DoF) that can be estimated by

$$\mathrm{DoF} = \begin{cases} (N-2) & \text{for} \quad d = 0 \\ \dfrac{(N-2)\delta}{2d} & \text{for} \quad d \geq \delta \end{cases} \tag{16}$$

The DoF is the ratio of the number of time intervals $N - 1$ minus 1 and the number of closely correlated samples in the

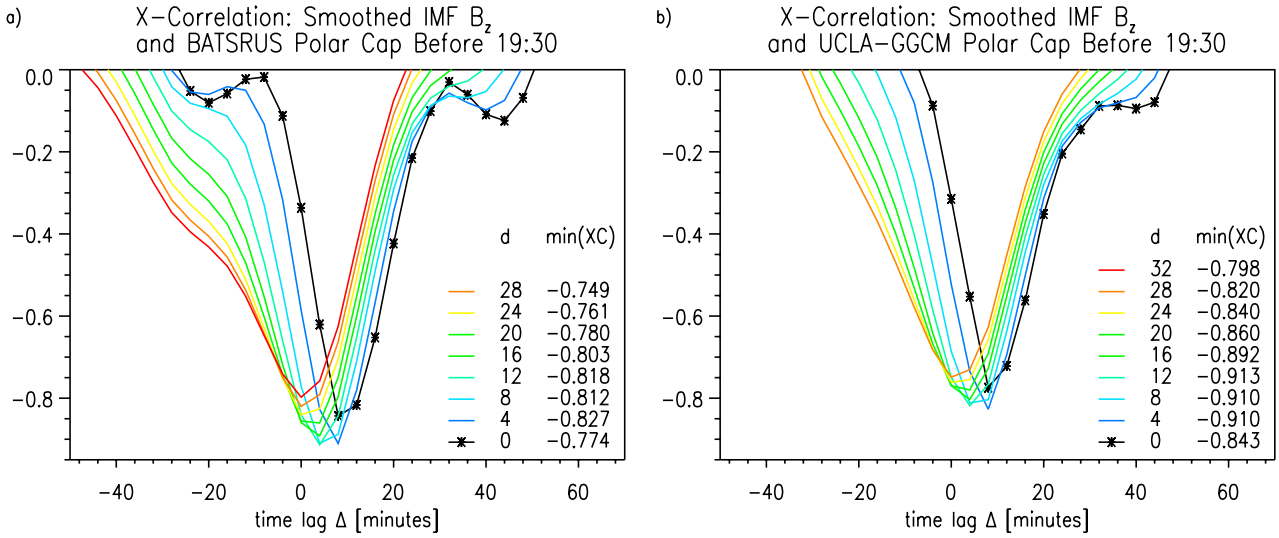

Figure 5. Cross-correlation of smoothed B_z and modeled polar cap sizes. Results from (a) the BATSRUS run with auroral conductances, using data before 1930 UT, and (b) the UCLA-GGCM run with CTIM are shown. The same IMF B_z smoothing timescales and time lag parameters have been used as in Figure 4 and the shorter period from 1400 UT to 1930 UT was used.

smoothed input $2d/\delta$ (or 1 for $d = 0$ without smoothing for random input to the smoothing). In our study, the samples are $\delta = 4$ min apart (IMAGE and Polar polar cap size data have been interpolated to the same interval from their spacing of 123 and 270 s between images, respectively) and d is ranging from 0 and 32 min in 4-min increments ($2d/\delta$ ranging from 0 to 16). From the statistic T_{XC} one can calculate the critical cross-correlation coefficient

$$XC_{\mathrm{crit}}(\alpha, \mathrm{DoF}) = \left(\frac{T_c^2}{\mathrm{DoF} + T_c^2}\right)^{0.5}, \qquad (17)$$

with T_c being the critical value of T_{XC} at confidence level of α (probability of error usually 5%) and degree of freedom DoF. Table 1 shows the critical cross correlations for the two time periods (1400 UT to 2400 UT and 1400 UT to 1930 UT) over the range of smoothing timescales d used.

[40] Table 2 shows the minimum correlation coefficients with their associated parameters d and Δ for the solar wind parameters with the observed and modeled polar cap sizes, both for the whole simulation time interval (1400 UT to 2400 UT) and the time between 1400 UT and 1930 UT. Table 2 shows the cross-correlation coefficients calculated for the two time periods between the solar wind parameters (left column) and either the polar cap size from IMAGE/Polar satellite observations, BATSRUS, and UCLA-GGCM simulations (the runs with auroral and CTIM conductances, respectively). The far right column shows autocorrelation timescales for each of the solar wind parameters (defined as the time delay Δ when $|XC|$ falls to 0.5).

[41] Of the solar wind parameters, B_z and ϵ have similar characteristics in terms of autocorrelation (large Δ_{AC} of 28 and 36 min for the whole time interval and short $\Delta_{\mathrm{AC}} = 8$ for the time before 1930 UT). The autocorrelation timescale drops as the large magnetic cloud with negative B_Z after 1930 is excluded. Autocorrelation timescales ΔAC of P_{dyn} (12–14 min) are similar to those of V_x (20 min) and N (15–16 min) which do not vary significantly between the two time intervals.

[42] The modeled polar caps (labeled "BATSRUS auroral" and "UCLA-GGCM CTIM") exhibit largest anticorrelation with the IMF B_z parameter, smoothed over relatively short timescales $d = 4$ min (both models and UCLA-GGCM before 1930 UT) or $d = 12$ min (BATSRUS, before 1930 UT), whereas the observed polar caps ("IMAGE/Polar") anticorrelate best with B_z smoothed over a longer time of over 20 min (28 min for time interval before 1930 UT). Minimum correlation coefficients do not change substantially between the two time intervals except for the XC obtained between the measured polar caps and B_z where the anticorrelation is much stronger with the shorter time interval. In all cases, the resulting delay time Δ is very similar (between 0 and 8 min) and averages the expected solar wind travel time from the upstream model boundary at 33 R_E (near the Geotail solar wind monitor position) and Earth of 4 min (at solar wind speed $V_x = 900$ km/s). Anticorrelation between ϵ and the polar cap are generally weaker than anticorrelation with B_z but show the same smoothing timescale and delays for the model runs ($d = 4$, $\Delta = 8$). Observed polar caps correlate weakly with ϵ for $d = 0$ and significance is lost before a minimum is found when

Table 1. Critical Cross-Correlations XC_{crit} Applicable to the Time Periods With Number of Samples N and Some of the Smoothing Timescales d Used in This Study[a]

1400 to 2400 UT				1400 to 1930 UT			
N	d	DoF	XC_{crit}	N	d	DoF	XC_{crit}
151	0	149.0	0.159	91	0	89.0	0.206
151	4	74.5	0.224	91	4	44.5	0.289
151	8	37.3	0.315	91	8	22.3	0.402
151	16	18.6	0.437	91	16	11.1	0.550
151	32	9.3	0.594	91	32	5.6	0.727

[a]The hypothesis that $XC \sim 0$ can be rejected with $\alpha = 5\%$ probability of error if $|XC| > XC_{\mathrm{crit}}$.

Table 2. Minimum Cross-Correlations *XC* of Various (Solar Wind) Inputs With Polar Cap Sizes (Observed and Modeled) and With Themselves (Autocorrelation)[a]

	Minimum XC Between Input Parameter									
	IMAGE/Polar			BATSRUS Auroral			UCLA-GGCM CTIM			AutoCorr. Timescale
Parameter	min(*XC*)	d^b	Δ	min(*XC*)	d^b	Δ	min(*XC*)	d^b	Δ	Δ_{AC}
B_z	−0.504	20[b]	8	−0.934	4[b]	8	−0.795	4[b]	8	∼28
B_z before 1930	−0.869	28[b]	0	−0.913	12[b]	4	−0.827	4[b]	8	8
ϵ	−0.300	4[b]	16	−0.766	4[b]	8	−0.586	0[b]	8	36
ϵ before 1930	−0.447	8[b]	12	−0.796	32[b]	0	−0.586	16[b]	0	8
P_{dyn}	−0.691	24[b]	0	−0.198	0[b]	20	−0.265	4[b]	16	12
P_{dyn} before 1930	−0.757	32[b]	−4	−0.477	4[b]	24	−0.525	12[b]	12	14
V_x	−0.358	4[b]	56	−0.302	4[b]	60	−0.384	4[b]	60	20
V_x before 1930	−0.725	12[b]	52	−0.472	0[b]	66	−0.488	4[b]	60	20
N	−0.732	24[b]	0	−0.272	4[b]	20	−0.324	4[b]	16	16
N before 1930	−0.789	32[b]	0	−0.512	4[b]	24	−0.531	8[b]	16	15

[a]Correlation coefficients are listed with the associated smoothing timescales *d* and time delays Δ as applicable for the full time period from 1400 UT to 2400 UT and the restricted time period from 1400 UT to 1930 UT. The auto-correlation timescales Δ_{AC} are defined here as the delay time when |*XC*| reaches 0.5.

[b]Significance is lost with larger *d*, i.e., $|\min(XC)\ (d,\Delta)| < XC_{crit}(d)$ (Table 1).

varying *d*. The differences of the delay times Δ found are within one sampling interval (of 4 min) around the average of 4 min. An analysis of reaction times in the magnetosphere would thus require modeled 3-D results and processed images at a much higher rate than was used for this study (e.g, every minute or every 30 s).

[43] Correlations between modeled polar cap sizes and solar wind dynamic pressure P_{dyn}, density *N*, and V_x are much weaker and loose significance altogether at small values of *d*, even for the smaller time period before 1930 UT for which the anticorrelations at $d = 0$ are generally stronger. Within the significant range of *XC*, the resulting delays Δ were larger (12–24 min for P_{dyn} and *N*) than those found for B_z (<= 8 min). The delays were inconsistent with those obtained for V_x (between 52 and 60 min). The observed polar caps again anticorrelated best when large smoothing times *d* were applied ($d > 24$ for P_{dyn} and *N*; $d = 12$ for V_X). Delay times Δ approach zero except for V_x for those large smoothings, similar to correlations with B_z.

[44] With the shorter time interval, the correlation coefficients as functions of Δ show much more pronounced minima in agreement with the reduced autocorrelation timescales of the solar wind parameters as seen in Figure 5b. The strong correlations of the observed and modeled polar cap sizes with parameters P_{dyn} and V_x in Table 2 occur due to the fact that polar cap sizes in the later times remain much bigger than in the beginning of the time period and the parameters follow a similar trend into the opposite direction. During quiet times with moderate IMF B_z before the first CME hits the magnetosphere, the polar caps derived from the MHD simulations agree well with the satellite observations (from IMAGE). During the dynamic periods, the MHD simu-

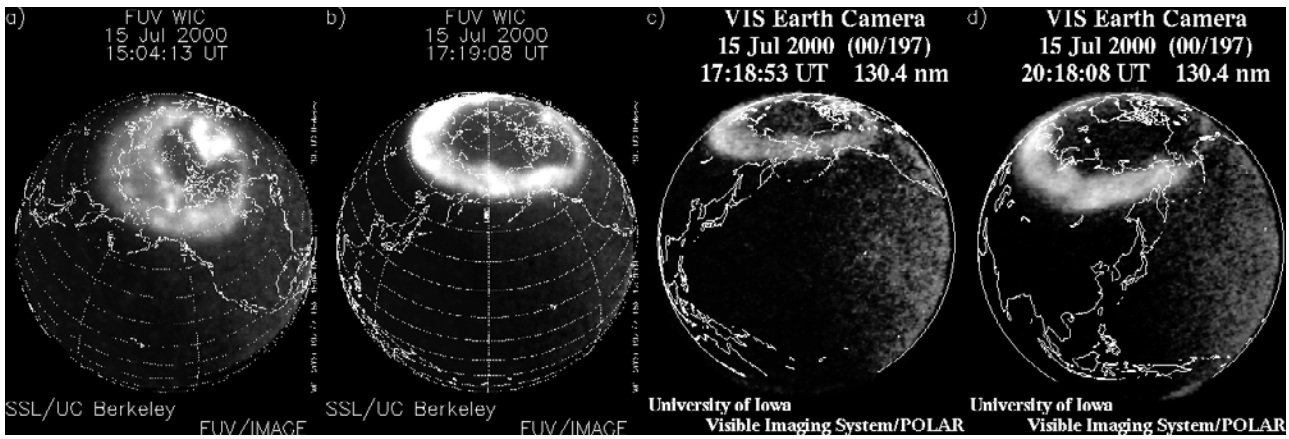

Figure 6. IMAGE FUV and Polar VIS images of polar cap. Full polar cap coverage is available from IMAGE before 1743 UT, shown for (a) 1504:13 UT when the polar cap size is minimal and (b) 1719:08 UT. After 1704 UT images from Polar cover the entire polar cap as Polar rises higher. Panel c was taken at 1718:53 UT (about the same time as Figure 6b and panel d at 2018:08 UT when the polar cap is at its maximum size. The images of Figures 6b and 6c were taken near the time of Figures 7b and 7e, and Figure 6d was taken near the time of Figures 7c and 7f.

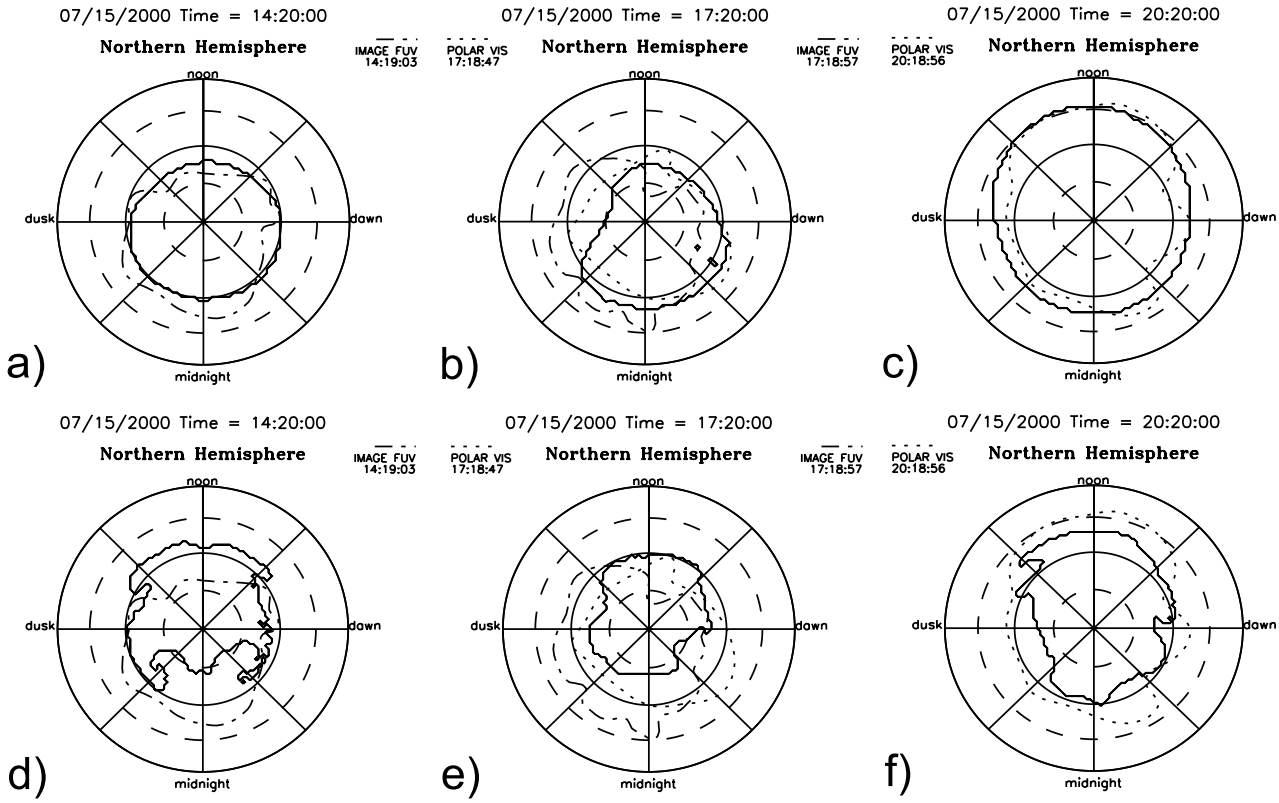

Figure 7. Polar cap locations. The polar cap location in the ionosphere as determined by the satellite measurements (dash-dotted represents IMAGE, while dotted represents Polar) and the model results BATSRUS with auroral conductances (Figures 7a, 7b,and 7c, top row) and UCLA-GGCM with CTIM conductances (Figures 7d, 7e,and 7f, bottom row) are shown for three times. Although polar cap sizes may agree well, the cap location or shape may differ considerably. Especially UCLA-GGCM exhibits a displacement of the cap location in early times of the run (Figures 7b and 7d). Notice that even between the two satellites, there is a certain discrepancy in shape and location (shown in Figures 7c and 7d for 1720 UT) although the respective cap sizes agree well at that time.

lations exhibited a weaker response compared to the degree of change of the polar cap size seen in the satellite observations from both IMAGE and Polar.

6.1. Polar Cap Location

[45] Although the polar cap size may agree in periods of moderate solar wind IMF, the precise shape and location may be different between the models and compared to the satellite observations. Figures 6a and 6b show the images acquired by IMAGE FUV for the early times. At about 1504:13 UT in Figure 6a, the polar cap (dark area poleward of the auroral oval) is at its smallest size. The image in Figure 6b taken at 1719:08 UT is one of the last FUV images showing the entire polar cap. As IMAGE moves closer to the equator it can observe only parts of the polar cap after 1743 UT. The first Polar image shown (Figure 6c, 1718:53 UT) was taken shortly after Polar has risen high enough to observe the entire polar cap. The viewing geometry is similar to the FUV image at the same time (Figure 6b) and the shape of the polar cap appears nearly identical. At 2018:08 UT the auroral oval has intensified and the polar cap is dramatically enlarged (Figure 6d).

[46] Figure 7 shows the polar caps north of 50 degrees northern latitude for two simulations with the data from the two satellites as available (see Figure 6). Three times of the BATSRUS run with auroral conductances are shown in the top row in Figures 7a, 7b, and 7c and the corresponding times in the UCLA-GGCM/CTIM run are shown in Figures 7d, 7e, and 7f. The times are 1420 UT (before the CME), 1720 UT (after northward turning of IMF B_z after first CME structure), and 2020 UT (at the beginning of prolonged period of southward IMF B_z), respectively.

[47] In general, the polar caps obtained with BATSRUS have a smooth edge and seem to agree a little better with the observed polar caps for some time periods. Polar caps calculated from UCLA-GGCM results show irregular edges not seen in BATSRUS simulations. The ragged nature of the appearance of the polar cap edge is seen in all UCLA-GGCM model runs. The causes are unclear at this time.

7. Summary and Discussion

[48] We have computed the polar cap boundary in the northern hemisphere defined as the boundary between open

and closed field lines in MHD simulations for the CME events of 15 July 2000. The MHD-calculated polar caps were compared with the UV emission-free regions in images from two satellites (IMAGE, Polar) usually being identified as the polar cap area [*Frank and Craven*, 1988]. During quiet times with moderate IMF B_z, before the first CME hits the magnetosphere, the polar cap sizes derived from the MHD simulations agree well with the satellite observations (from IMAGE). During the dynamic periods, the MHD simulations exhibited a weaker response compared to the degree of change of the polar cap size seen in the satellite observations from both IMAGE and Polar.

[49] In the first dynamic time interval from 1445 to 1720 the changes of the polar cap size in the MHD simulation was about 50% of the changes seen by the IMAGE satellite. The observed polar cap ranges in size from $1.6 \cdot 10^{12}$ m^2 at 1520 (with strong northward IMF B_z) to more than $2.6 \cdot 10^{13}$ m^2 after a southward turning of the IMF (at around 1700 UT). Whereas the MHD simulations exhibit very similar rates of shrinkage (expansion) of the polar cap after northward (southward) turnings of the IMF, the effective range of variations remains much smaller (between $5 \cdot 10^{12}$ m^2 and $2 \cdot 10^{13}$ m^2 before about 1920 UT).

[50] After 1726 UT, a small period of southward B_z caused a rapid increase of polar cap size computed by the MHD model whereas the satellite images do not detect an increase of the polar cap size. This indicates that the simulated state of the magnetosphere in MHD models depend more strongly on recent IMF input.

[51] Later during the day, as polar cap sizes observed by Polar rise up to $3.0 \cdot 10^{13}$ m^2 (after 2000 UT), the model results start differing dramatically. BATSRUS simulations eventually reach polar cap sizes comparable to the observations (over $2.5 \cdot 10^{13}$ m^2 between about 2000 UT and 2100 UT) and over $2.0 \cdot 10^{13}$ m^2 for the entire time after about 1920 UT. UCLA-GGCM polar caps remain much smaller (between $1.2 \cdot 10^{13}$ m^2 and $1.9 \cdot 10^{13}$ m^2 between 1920 and 2130) and below $1.2 \cdot 10^{13}$ m^2 after 2130 UT.

[52] BATSRUS polar cap sizes track the changes in IMF B_z much more closely than UCLA-GGCM simulations. To quantify the way the models reproduce the observed polar caps when given the same solar wind input, we use cross-correlation coefficients calculated between the modeled polar cap sizes and several solar wind parameters (IMF B_z, Akasofu ϵ, solar wind dynamic pressure, velocity V_x, and density N). We also compute correlation coefficients between the observed polar cap size data and the same solar wind parameters to obtain an idea of the reaction of the magnetosphere system. Exponential smoothing was used to find estimates of about 20 to 28 minutes for the "memory" timescales of the magnetosphere system in nature and of 4 to 8 min for the magnetosphere as modeled by the BATSRUS and UCLA-GGCM models. Chance correlations were eliminated by using a T-distributed statistic by estimating the degree of freedom from the time interval and smoothing time.

[53] The Akasofu ϵ exhibits similar correlations due to its connection to B_z (Table 2). Only weak correlations have been found between the solar wind density and dynamic pressure and the polar cap sizes from the model results for the full time periods. Significance is lost when increasing d beyond 4 min. For the time before 1930 UT, significance is higher but delay times seem unreasonably high for V_x (52–66 min). The observed polar cap exhibit significantly stronger correlations with the solar wind density and dynamic pressure than the simulations and indicate larger memory time d of between 24 and 32 min, similar to cross-correlations with B_z. Within the limits of statistical significance, all solar wind parameters seem to correlate better with larger memory intervals than the model results.

[54] The cross-correlation coefficients calculated for this event are only a beginning of a more extensive study that must involve multiple storm events. Correlations between the solar wind parameters during a storm event have to be considered in addition to the correlations to observed and modeled magnetospheric features in order to obtain conclusive results on the behavior of the magnetospheric system.

[55] Comparing the locations of the observed polar caps and the model results show that the modeled polar cap boundaries can deviate up to 10 degrees from the observed boundaries in some instances, even when the cap size seem to agree well. At some times, the agreement between observation and model can be fairly good (to within 3 degrees), but they might be coincidental as they usually do not last for more than a few time steps (intervals of 4 min between 3-D outputs in this study). On the other hand, in the case of the overlap interval between 1705 UT and 1745 UT, we also note a considerable discrepancy in the location of polar cap features seen by the two satellite imagers, although in general the polar cap sizes seem to agree fairly well. Uncertainties of the height from where emissions emanate together with the different viewing angles can produce projection errors that contribute to the shift of the emission-free region between different imagers looking at the same region. It has yet to be determined with the help of other observations under which conditions a given image provides good "ground truth" to compare against model results.

[56] Approximations such as $B_x = 0$ and $\frac{\partial}{\partial y} = \frac{\partial}{\partial z} = 0$ have been used at the upstream boundary of the simulation box as data were only available from single-satellite measurements of plasma and magnetic field properties in the upstream solar wind. The correct positioning and size of the polar cap can easily be lost in the simulations during this event where all components of the IMF varied strongly and B_x at times was comparable to the other IMF components.

[57] Other factors may also contribute to discrepancies. For example, reconnection rates in MHD that are responsible for fast magnetic topology changes have been found to be too low compared with Hall-MHD, hybrid, or full kinetic models in the GEM reconnection challenge [e.g., *Birn et al.*, 2001, and references therein]. The low reconnection rates may also result from the lack of fine structures and current densities resolved in large-scale MHD simulations together with the neglected corrections to the ideal MHD equations related to those unresolved spatial scales. The reduced reconnection rates in global MHD create smaller dynamic changes to the polar cap size during the first time period. The limited spatial resolution artificially raises the level of background dissipation, which is implicitly included in the shock-capturing scheme used by the BATSRUS and the UCLA-GGCM models. This causes premature reconnection (especially in the near-Earth magnetotail), which might be enhanced in UCLA-GGCM simulations by the current-driven resistivity employed by that model. MHD reconnection in the near-Earth

magnetotail current sheet that limits the tail length was studied in detail during the Geospace Environment Modeling substorm challenge [*Raeder et al.*, 2001b; *Slinker et al.*, 2001]. Owing to premature tail reconnection, the tail flux buildup creating a large polar cap is limited when subsolar reconnection is supposed to be larger than tail reconnection during long time periods with strongly southward IMF. The polar cap observed is thus larger than calculated by MHD until a storm or substorm event unloads the tail flux and reduces the polar cap to be more in line with model results. Another possible factor that can influence model results, the conductance model used in the ionosphere of a simulation, did not change the polar cap sizes much.

[58] MHD models are able to reproduce global-scale changes in the polar cap reasonably well, whereas detailed structures along the polar cap boundaries such as individual arcs that are sometimes seen in emission images cannot be reproduced with the current degree of spatial resolution of the coupled magnetosphere-ionosphere models. Substantial improvements are still needed to make the models accurate enough to model effects seen in the ionosphere such as auroral emissions and to predict correct magnetospheric events during a large dynamic event such as the Bastille Day event of 2000.

[59] **Acknowledgments.** This work was supported by the NASA Space Physics Theory Program and was performed within the framework of the Community Coordinated Modeling Center (CCMC), supported by NASA, AFMC, AFOSR, AFRL, AFWA, NOAA, and NSF. Computations were performed on CCMC's Beowulf systems at NASA Goddard. Emission boundary data computed from images from the IMAGE WIC-FUV and Polar VIS Earth Camera data were provided by S.B. Mende of UC Berkeley and J.B. Sigwarth of the Univ. of Iowa (now at NASA GSFC), respectively. Geotail (CPI) plasma and magnetic field (MGI) data were obtained through CDAWeb (http://cdaweb.gsfc.nasa.gov). The computations were performed as science-based evaluation of the model within the Community Coordinated Modeling Center (CCMC, http://ccmc.gsfc.nasa.gov/). The UCLA-GGCM work was supported by NSF grant ATM-0353211 and NASA grant NAG5-12107.

[60] Lou-Chuang Lee thanks Joseph Huba and Benoit Hubert for their assistance in evaluating this paper.

References

Axford, W. I., and C. O. Hines (1961), A unifying theory of high-latitude geophysical phenomena, *Can. J. Phys.*, *39*, 1433.

Bailey, G. J., and N. Balan (1996), *STEP Handbook of Ionospheric Models*, edited by R. W. Shu, pp. 173–206, Utah State Univ., Logan, Utah.

Birn, J., M. A. Shay, B. N. Rogers, R. E. Denton, M. Hesse, M. Kuznetsova, Z. W. Ma, A. Bhattacharjee, A. Otto, and P. L. Pritchett (2001), Geospace Environmental Modeling (GEM) Magnetic Reconnection Challenge, *J. Geophys. Res.*, *106*, 3715.

Boris, J. P. (1970), A physically motivated solution of the Alfvén problem, *Tech. Report NRL Memo. Rep. 2167*, Naval Res. Lab., Washington, D.C.

Dungey, J. W. (1961), Interplanetary magnetic field and the auroral zones, *Phys. Rev. Lett.*, *6*, 47.

Frank, L. A., and J. D. Craven (1988), Imaging results from Dynamics Explorer 1, *Rev. Geophys.*, *26*(2), 249.

Frank, L. A., and J. D. Sigwarth (2003), Simultaneous images of the northern and southern auroras from the polar spacecraft: An auroral substorm, *J. Geophys. Res.*, *108*(A4), 8015, doi:10.1029/2002JA009356.

Frank, L. A., K. L. Ackerson, W. R. Paterson, R. L. Dyson, G. T. Parmentier, and G. L. Pickett (1994), GEOTAIL comprehensive plasma instrumentation (CPI), *J. Geomagn. Geoelectr.*, *46*, 23.

Frank, L. A., J. D. Sigwarth, J. D. Craven, J. P. Cravens, J. S. Dolan, M. R. Dvorsky, J. D. Harvey, P. K. Hardebeck, and D. Muller (1999), The visible imaging system (VIS) for the POLAR spacecraft, *J. Geophys. Res.*, *104*, 14,557.

Goodman, M. L. (1995), A three-dimensional, iterative mapping procedure for the implementation of an ionosphere-magnetosphere anisotropic (Ohm's) law boundary condition in global magnetohydrodynamic simulations, *Ann. Geophys.*, *13*, 843.

Gombosi, T. I., G. Tóth, D. L. DeZeeuw, K. G. Hansen, K. Kabin, and K. G. Powell (2002), Relativistic magnetohydrodynamics and physics-based convergence acceleration, *J. Comput. Phys.*, *177*, 176.

Hauptmann, J. M. (1994), Simulation of physical systems, in *Statistical Methods for Physical Science*, edited by J. L. Stanford and S. B. Vardeman, p. 464, Elsevier, New York.

Hedin, A. E. (1987), MSIS-86 thermosphere model, *J. Geophys. Res.*, *92*, 4649.

Jordanova, V. K., R. M. Thorne, C. J. Farrugia, Y. Dotan, J. F. Fennel, M. F. Thomsen, G. D. Reeves, and D. J. McComas (2001), Ring current dynamics during the 13–18 July 2000 storm period, *Solar Phys.*, *204*, 361.

Kokubun, S., T. Yamamoto, M. H. Acuna, K. Hayashi, K. Shiokawa, and H. Kawano (1994), The Geotail magnetic field experiment, *J. Geomagn. Geoelectr.*, *46*, 7.

Lepping, R. P., et al. (2001), The Bastille Day magnetic clouds and upstream shocks: Near-Earth interplanetary observations, *Solar Phys.*, *204*, 287.

Liu, R. Y., Y. H. Liu, Z. H. Xu, N. Sato, and B. J. Fraser (2001), Responses of the polar ionosphere to the Bastille Day solar event, *Solar Phys.*, *204*, 307.

McPherron, R. L. (1991), Physical processes producing magnetospheric substorms and magnetic storms, in *Geomagnetism-4*, edited by J. Jacobs, p. 593, Elsevier, New York.

Mende, S. B., H. U. Frey, M. Lampton, J. C. Gerard, B. Hubert, S. Fuselier, J. Spann, R. Gladstone, and J. L. Burch (2001), Global observations of proton and electron auroras in a substorm, *Geophys. Res. Lett.*, *28*, 1139.

Mende, S. B., H. U. Frey, T. J. Immel, J. C. Gerard, B. Hubert, and S. Fuselier (2003), Global imaging of proton and electron aurorae in the far ultraviolet, *Space Sci. Rev.*, *109*(1-4), 211.

Powell, K. G., P. L. Roe, T. J. Linde, T. I. Gombosi, and D. L. DeZeeuw (1999), A solution-adaptive upwind scheme for ideal magnetohydrodynamics, *J. Comput. Phys.*, *154*(2), 284.

Raeder, J. (1999), Modeling the magnetosphere for northward interplanetary magnetic field: Effects of electrical resistivity, *J. Geophys. Res.*, *104*, 17,357.

Raeder, J. (2003), Global geospace modeling: Tutorial and review, in *Space Plasma Simulation*, edited by J. Büchner, C. T. Dum, and M. Scholer, p. 212, Springer, New York.

Raeder, J., R. L. McPherron, L. A. Frank, S. Kokubun, G. Lu, T. Mukai, W. R. Paterson, J. B. Sigwarth, H. J. Singer, and J. A. Slavin (2001a), Global simulation of the Geospace Environment Modeling substorm challenge event, *J. Geophys. Res.*, *106*(A1), 381.

Raeder, J., Y. Wang, and T. Fuller-Rowell (2001b), Geomagnetic storm simulation with a coupled magnetosphere-ionosphere-thermosphere model, in *Space Weather*, *Geophys. Mongr. Ser.*, vol. 125, edited by P. Song, G. Siscoe, and H. J. Singer, AGU, Washington, D. C.

Raeder, J., Y. L. Wang, T. Fuller-Rowell, and H. J. Singer (2001c), Global simulation of magnetospheric space weather effects of the bastille day storm, *Solar Physics*, *204*, 325.

Rastätter, L., M. Hesse, M. Kuznetsova, T. I. Gombosi, and D. L. DeZeeuw (2002), Magnetic field topology during July 14–16 (Bastille Day) solar CME event, *Geophys. Res. Lett.*, *29*(15), 1747, doi:10.1029/2001GL014136.

Ridley, A. J., D. L. DeZeeuw, T. I. Gombosi, and K. G. Powell (2001), Using steady-state mhd results to predict the global state of the magnetosphere ionosphere system, *J. Geophys. Res.*, *106*, 30,067.

Roble, R., and E. Ridley (1994), A Thermosphere-Ionosphere-Mesosphere-Electrodynamics General-Circulation Model (Time-GCM): Equinox solar cycle minimum simulations (30–500 km), *Geophys. Res. Lett.*, *21*, 417.

Slinker, S. P., J. A. Fedder, J. M. Ruohoniemi, and J. G. Lyon (2001), Global MHD simulation of the magnetosphere for November 24, 1996, *J. Geophys. Res.*, *106*, 361.

Smith, C. W., et al. (2001), ACE observations of the Bastille Day 2000 interplanetary disturbances, *Solar Phys.*, *204*, 229.

Sonnerup, B. U. O., and L. J. Cahill (1967), Magnetopause structure and attitude from Explorer 12 observations, *J. Geophys. Res.*, *72*, 171.

Sonnerup, B. U. O., and L. J. Cahill (1968), Explorer 12 observations of the magnetopause current layer, *J. Geophys. Res.*, *73*, 1757.

Walker, R. J., T. Ogino, J. Raeder, and M. Ashour-Abdalla (1993), A global magnetohydrodynamic simulation of the magnetosphere when the interplanetary field is southward: The onset of magnetotail reconnection, *J. Geophys. Res.*, *98*, 17,235.

T. I. Gombosi, Department of Engineering, Space Research Building, University of Michigan, 2455 Hayward Street, Ann Arbor, MI 48109-2143, USA.

M. Hesse, M. Kuznetsova, L. Rastätter, and J. B. Sigwarth, Code 696, NASA Goddard Space Flight Center, Greenbelt, MD 20771, USA. (lr@waipio.gsfc.nasa.gov)

J. Raeder, Space Science Center, University of New Hampshire, 39 College Road, Durham, NH 03824-3525, USA.